# Effective versus ion thermal temperatures in the Weizmann Ne Z-pinch: Modeling and stagnation physics

J. L. Giuliani,[1] J. W. Thornhill,[1] E. Kroupp,[2] D. Osin,[2] Y. Maron,[2] A. Dasgupta,[1] J. P. Apruzese,[3] A. L. Velikovich,[1] Y. K. Chong,[1] A. Starobinets,[2] V. Fisher,[2] Yu. Zarnitsky,[2] V. Bernshtam,[2] A. Fisher,[4] T. A. Mehlhorn,[1] and C. Deeney[5]
[1]*Plasma Physics Division, Naval Research Laboratory, Washington, DC 20375, USA*
[2]*Weizmann Institute of Science, Rehovot 76100, Israel*
[3]*Consultant to NRL through Engility Corp., Chantilly, Virginia 20151, USA*
[4]*Falculty of Physics, Technion-Israeli Institute of Technology, Haifa, Israel*
[5]*National Security Technologies, LLC, Las Vegas, Nevada 89144, USA*

(Received 23 August 2013; accepted 22 October 2013; published online 28 February 2014)

The difference between the ion thermal and effective temperatures is investigated through simulations of the Ne gas puff z-pinch reported by Kroupp *et al.* [Phys. Rev. Lett. **107**, 105001 (2011)]. Calculations are performed using a 2D, radiation-magnetohydrodynamic code with Tabular Collisional-Radiative Equilibrium, namely Mach2-TCRE [Thornhill *et al.*, Phys. Plasmas **8**, 3480 (2001)]. The extensive data set of imaging and K-shell spectroscopy from the experiments provides a challenging validation test for z-pinch simulations. Synthetic visible images of the implosion phase match the observed large scale structure if the breakdown occurs at the density corresponding to the Paschen minimum. At the beginning of stagnation (−4 ns), computed plasma conditions change rapidly showing a rising electron density and a peak in the ion thermal temperature of ∼1.8 keV. This is larger than the ion thermal temperature (<400 eV) inferred from the experiment. By the time of peak K-shell power (0 ns), the calculated electron density is similar to the data and the electron and ion thermal temperatures are equilibrated, as is observed. Effective ion temperatures are obtained from calculated emission line widths accounting for thermal broadening and Doppler velocity shifts. The observed, large effective ion temperatures (∼4 keV) early in the stagnation of this Ne pinch can be explained solely as a combination of compressional ion heating and steep radial velocity gradients near the axis. Approximations in the modeling are discussed in regard to the higher ion thermal temperature and lower electron density early in the stagnation compared to the experimental results. © *2014 AIP Publishing LLC*. [http://dx.doi.org/10.1063/1.4865223]

## I. INTRODUCTION

In a z-pinch, the voltage across a wire array or gas puff initiates a breakdown, whereupon the axial current ($J_z$) through the plasma produces an azimuthal magnetic field ($B_\varphi$), and the resultant inward radial force ($\propto J_z \times B_\varphi$) compresses the material onto the axis. During the implosion, the plasma accelerates and acquires kinetic energy that is subsequently converted to internal energy during stagnation. The physics of stagnation and thermalization is of keen interest whether the application is K-shell radiation sources,[1] neutron sources,[2] or pinch driven hohlraums for inertial confinement fusion.[3]

Spectroscopic diagnostics have played a central role in analyzing the plasma conditions at stagnation. The electron temperature and density have long been determined from line ratios and absolute intensities of K-shell spectra,[4] or more recently from L-shell emission.[5] The ion temperature is also a fundamental quantity because the kinetic energy dissipates as ion heat followed by equilibration with the electrons. But diagnosis of the ion temperature has been much less frequent than that of the electron temperature. Table I contains reported ion temperatures from the extant literature.[6–12] The top four rows give the reference, the generator, the peak load current, and the load material. The electron density ($n_e$), electron temperature ($T_e$), and the effective ion temperature ($T_i^{eff}$) are conditions of the stagnated plasma. In all cases, $T_i^{eff}$ was determined from the Doppler width of H- or He-like spectral lines using high resolution spectroscopy. Interestingly, over the range of currents from 0.5 to 15 MA, $T_i^{eff}$ exceeds $T_e$ by more than an order of magnitude. However, it is controversial whether $T_i^{eff}$ is the same property as the ion thermal temperature ($T_i$).

Several conjectures have been offered to explain the large discrepancy between $T_e$ and $T_i^{eff}$, and the physics of the latter quantity. In the earliest report, Wong *et al.*,[7] found that their 2D simulation of Ar-Ne implosions on the Saturn generator produced ion thermal temperatures that were much lower than the observed $T_i^{eff}$. They attributed the difference to 3D hydrodynamics such as convective mixing, angular rotation, or "small scale turbulence." A completely different explanation was presented by Haines *et al.*,[13] who suggested that $T_i^{eff}$ does represent a thermal distribution and it is driven by viscous heating resulting from the dynamics of the $m = 0$ magnetohydrodynamic (MHD) instability. Based on scaling arguments for this process, the magnetic field is required to be frozen in the plasma over a length scale for which the momentum is diffusive, i.e., the magnetic Prandtl number

 

TABLE I. Compilation by published date of the electron density ($n_e$), temperature ($T_e$), and effective ion temperatures ($T_i^{eff}$) measured at stagnation for z-pinches of various materials on denoted generators of peak load current ($I$). The charge state is inferred from the data in the references and $P_{r,m}$ is the computed Prandtl number.

| Reference No. | 6 | 7 | 8 | 9 | 10 | 11 | 12 |
|---|---|---|---|---|---|---|---|
| Generator | Saturn | Saturn | Double Eagle | Z | WIS[a] | Qiang-Guang-I | WIS[a] |
| $I$ (MA) | 7 | 8 | 3.5 | 15 | 0.32 | 1.5 | 0.5 |
| Material | Al | Ne/Ar | Ar | SS | Ne | Al | Ne |
| $n_e$ (1/cm$^3$) | $3.7 \times 10^{21}$ | $2.1 \times 10^{21}$ | $8.4 \times 10^{20}$ | $2.5 \times 10^{21}$ | $2 \times 10^{20}$ | $6 \times 10^{20}$ | $6 \pm 3 \times 10^{20}$ |
| $T_e$ (keV) | 1.4 | 1.2 | 1.01 | 3.0 | 0.25 | 0.28 | 0.2 |
| $T_i^{eff}$ (keV) | 66 | 36 | 19.8 | 200 | 2.3 | 10.2 | 3.8 |
| $Z$ | 12.5 | 9 | 16 | 25 | 9 | 11 | 9 |
| $P_{r,m}$ | 57 | 67 | 2.9 | 166 | 0.13 | 0.78 | 0.24 |

[a]WIS is the Weizmann Institute of Science.

(ion viscosity/magnetic diffusivity) must be large.[13] The last row in Table I shows that this condition is met at the largest currents, but not at the smaller ones where $T_i^{eff}$ still exceeds $T_e$. A complete theory for this heating mechanism has yet to be developed. Kroupp *et al.*[12] argued that the time scale for ion-electron thermal equilibration was $< 1$ ns in their experiment, much shorter than the duration of $T_i^{eff}$ exceeding $T_e$. They concluded that the true ion thermal temperature is close to $T_e$, and $T_i^{eff}$ has a large motion component, but "the nature of the hydrodynamic motion that dominates the ion kinetic energy at stagnation is not clear as yet."

The investigation of $T_i^{eff}$ by Kroupp *et al.*[12] using the 500 kA generator at the Weizmann Institute of Science (WIS) is of special interest because of the extensive data set obtained on that experiment with Ne gas puffs. For the implosion phase, there are multiple visible images revealing the gross morphology of the dynamics.[14] For the stagnation phase, a Ne K-shell hot spot forms at a repeatable axial location. Besides the K-shell pulse for this region, one has the temporal evolution of the K-shell emission radius, the electron density, the electron temperature, the ion thermal temperature, and the effective ion temperature. All of this information provides a challenge and an opportunity for validating simulation codes that incorporate the non-linear interaction between MHD, atomic physics, and non-local thermodynamic equilibrium (LTE) radiation transport in z-pinches: particularly challenging since the K-shell yield from this hot spot is estimated to be only ~2% of the total radiated yield.

The present paper presents simulations of the Ne pinch at WIS using Mach2-TCRE, a 2D, non-LTE, radiation-MHD simulation code with Tabular Collisional-Radiative Equilibrium (TCRE). We find that the observed structure in the visible images of the implosion phase can be reproduced by the simulations if breakdown is assumed to occur at the radius where the density reaches the Ne Paschen minimum, rather than the largest radius where gas from the nozzle is measured. During stagnation, the simulation results are comparable with much of the experimental data. The notable exceptions are the electron density and ion thermal temperature, which are computed to vary rapidly early in the stagnation, unlike the measurements of these two quantities. The calculated $T_i^{eff}$ from synthetic emission line profiles, which include thermal broadening and Doppler velocity shifts, agree with the experimental data. We conclude, at least for this Ne gas puff, that the large effective ion temperatures are not due to 3D effects or turbulence, but can be explained by steep gradients in the radial velocity near the axis and rapid ion heating at stagnation.

The next section describes the experiment, with emphasis on the initial gas distribution, and a brief review of the diagnostics. Section III contains a description of the simulation code. Section IV presents the simulation results divided into the implosion and stagnation phases. The discussion of the last section focuses on the physics of stagnation as drawn from the simulations, particularly how the ion thermal temperature differs, but the ion effective temperature agrees with the data. Approximations intrinsic to the simulations, and their impact on the computed results in comparison with the measured electron density and ion thermal temperature are discussed at the end.

## II. EXPERIMENT AND DIAGNOSTICS

The pulsed power driver at WIS used for the z-pinch under study includes a 5.5 $\mu$F capacitor charged to 60 kV with a resistance of 20 m$\Omega$ and a self inductance of 30 nH. It is terminated by the gas puff load with an anode-cathode gap of 9 mm ($z = 0$ at the cathode). The cathode is a gas nozzle that produces a central jet and an outer shell ~38 mm in diameter and the anode is a screen. The initial load inductance is ~4 nH, much less than the self inductance of the driver. The capacitor is discharged about 70 $\mu$s after the pin trigger signal to open the nozzle. The density distribution of the Ne gas puff at the discharge time, $n^o(r,z)$, is measured by planar laser induced fluorescence (PLIF) at six axial ($z$) and twenty-eight radial ($r$) positions on each side of $r = 0$. We have averaged the two radial sides and performed a bi-cubic spline interpolation of the PLIF data to specify the density over the $r$-$z$ computational domain. The PLIF measurements are calibrated by chordal interferometry, but the absolute density is uncertain to ~15%. We uniformly scaled the density within this range to agree with the measured implosion times. The resulting $n^o(r,z)$ is shown in Fig. 1 along with its relation to the load geometry. There are some features of this distribution relevant to the gas breakdown and morphology of the implosion discussed later. First, due to the delay

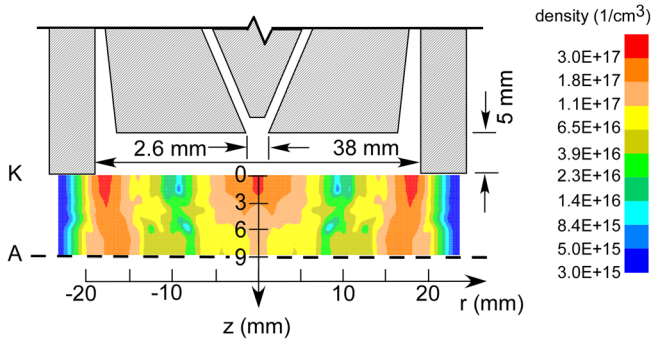


FIG. 1. Schematic diagram of the gas puff nozzle at the Weizmann Institute of Science and colored contours of the PLIF measured Ne density after averaging the data on the two sides of the axis and interpolating. The cathode is at $z = 0$.

between the opening of the nozzle valve and the capacitor discharge, the density extends out to a radius of ~23.5 mm, i.e., beyond the 19 mm of the nozzle radius. Second, the capacitor is discharged during the linearly rising history of the mass flow from the nozzle. At this time, the measured line mass density $[m^o(z) = \int_0 \rho^o(r,z) 2\pi r dr]$ is increasing at a rate of ~1.5 ($\mu$g/cm)/$\mu$s. Since the gas transit time across the gap is ~10 $\mu$s, $m^o(z)$ decreases linearly by ~20% from the cathode (~70 $\mu$g/cm) to the anode.

Numerous experiments for the same initial conditions indicate that the observed properties were fairly repeatable shot-to-shot and thereby facilitated high quality data with good signal-to-noise through repetitive measurements. An extensive data set was obtained from which the dynamics and state of the plasma could be inferred. The peak current varied within $520 \pm 20$ kA with implosion times ranging over $500 \pm 20$ ns, as measured from the time the capacitor discharged to the peak of the K-shell power. Since the implosion time is much smaller than the gas transit time across the gap, the mass loading in the gap can be considered fixed during the pinch.

The visible imaging throughout the implosion showed remarkable azimuthal symmetry and flaring arcs on the cathode side.[14] The remaining data, all time dependent, focused on the stagnation and intense K-shell emission from the region $0.4 < z < 0.6$ cm.[12] The absolute K-shell power pulse was obtained from filtered photo conducting diodes (PCDs). The radius of the K-shell emitting region was measured from x-ray imaging. The electron density was based on the ratio of Ly$_\alpha$ $^3P$ satellite lines. Collisional-radiative modeling along with the K-shell pulse provided the electron temperature. The effective ion temperature was determined from the line width of the Ly$_\alpha$ $^1D$ satellite line. There is little Stark broadening for this line. The thermal ion temperature was inferred from the ion-electron equilibration rate using the data for $T_e$ and $T_i^{eff}$.

## III. MODEL AND RESULTS

The Mach2-TCRE code was used to simulate the Ne z-pinch. Mach2 is an Arbitrary Lagrangian-Eulerian, 2D, MHD code.[15] To model the z-pinch we run the code in the $r$-$z$ mode with $128 \times 128$ zones. On each step the Langrangian push is followed by a remap to a rectilinear grid, but we employed a moving grid such that coordinate lines of the radial grid compress along with the pinch to resolve the implosion. Within the plasma the code uses the classical Spitzer resistivity and ion-electron equilibration rate for the transport coefficients. At the Naval Research Laboratory we have added several components to the basic code in order to model z-pinches. First, we have incorporated a circuit model that is non-linearly coupled to the changing inductive and resistive load voltage. Second, as Mach2 solves separate equations for the ion and electron temperatures, rather than a total energy conservation equation, it uses an artificial viscosity to capture shock fronts. Here, we have used the self-similar magnetized Noh solution as a verification test for pinch simulations to optimize the form of the artificial viscosity.[16] The most significant addition to the Mach2 code is the TCRE component, which treats the non-LTE character of the plasma. This is fully described in Thornhill *et al.*[17] Basically, a TCRE data base is a three dimensional table specified by density; internal energy (thermal plus ionization/excitation); and size. This size does not refer to the simulation zone size but rather relates to the optical depth, or equivalently the probability-of-escape, for a dominant emission line from each ionic stage. If a photon can escape from the emitting zone, it does not mean that it escapes from the whole plasma as it could be absorbed by neighboring, or even distant, zones. To account for this process, we also incorporated a discrete ordinates approach for the transport of each dominant emission line in 3D throughout the whole plasma. Specifically, the $EQ_4$ set is used with 24 rays projected from each zone. Note that these rays are not coordinate aligned to avoid biasing along the longest and shortest paths to escape. The transport technique uses probability-of-escape formalism, frequency averaged over the emission line, and was verified in recent papers.[18,19] For the calculations presented below, we have employed the on-the-spot approximation,[20] which states that if a photon is absorbed anywhere along a ray it is taken to be absorbed within the emitting zone. This approximation accounts for the non-local effect of radiation transport but applies the photo-trapping to the local population kinetics.

The Ne atomic model used to construct our TCRE data table is based on detailed configuration accounting and includes structure in all ionization stages with a total of 445 levels. The radiative output is determined from 803 emission lines, in particular 68 in H-like, 100 in He-like, and 58 in Li-like. The atomic processes for the population kinetics that couple the ground and excited levels to one another were calculated from the FAC code.[21] They include collisional excitation, and ionization, and their inverse processes, de-excitation and 3-body recombination. Likewise for photo-ionization and radiative recombination, and photo-pumping to excited levels and radiative decay. Dielectronic recombination rate coefficients were calculated using the autoionization and radiative rates from each doubly excited state and then lumped for the ionization kinetics in the TCRE tables.

### A. Implosion morphology

The gross dynamics of the implosion phase are revealed by the visible images of Ref. 14. Synthetic images of the

implosion were calculated by performing radiation transport for bremsstrahlung emissivity and absorptivity in the visible region based on the densities and temperatures of the simulation. A side-by-side comparison is shown in Fig. 2 for four times during the implosion, with time zero denoting the time of peak K-shell emission. We initially began with the density distribution shown in Fig. 1 covering the full radial range out to 23.5 mm. However, the visible morphology at the time of peak K-shell emission was quite different from that of the data. This is shown in Fig. 3 where one sees an image dominated by spikes instead of the single large flair on the cathode side as seen in the observations on the left of Fig. 2. To match the experiment we found that more realistic images resulted if the breakdown of the gas occurred at the Paschen minimum. The Paschen condition for breakdown in Ne is $\sim$4 cm $\times$ Torr, or $1.5 \times 10^{17}$ cm$^{-3}$ for the 9 mm A-K gap.[22] Reference to Fig. 1 indicates that this density occurs near the 20 mm radius. The synthetic images on the right of Fig. 2 are based on the implosion simulation from this position inward. We refer to this simulation with the breakdown at 20 mm as run A. It has a peak current of 544 kA, slightly larger than the average in the data (520 $\pm$ 20 kA), while the implosion time from the discharge (485 ns) is within the range in the data mentioned above. Run B refers to the simulation including the gas profile out to a radius of 23.5 mm.

Fig. 4 highlights the extreme sensitivity of the implosion visible morphology to the breakdown position assumed in runs A and B. The dashed curve labeled $m^o(z,B)$ shows the initial line density for run B, which includes the entire mass flow. As discussed in Sec. II, this line density decreases linearly with distance from the cathode. Correspondingly, the thin solid curve labeled $m^o(z,A)$ is the initial line mass density for run A. Because this line density is only evaluated out to 20 mm and because of the density structure evident in Fig. 1, $m^o(z,A)$ is not quite linear with $z$, but rather falls off slightly faster toward the anode. The value of $m^o(z,B)$ is slightly less than $m^o(z,A)$, because the larger initial radius of

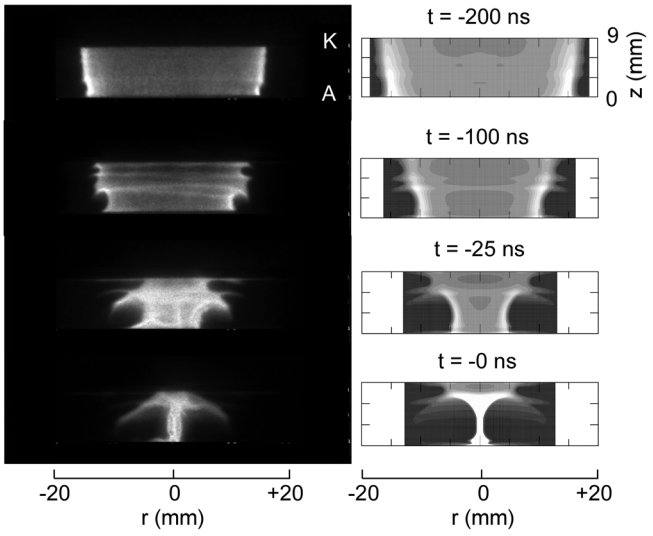


FIG. 2. Experimental visible images (left) of the Ne pinch implosion from Ref. 14 and synthetic images (right) from simulation run A at the times relative to that of peak K-shell emission. The simulated pinch was initiated (breakdown) at the Paschen minimum near the radius of 20 mm in Fig. 1.

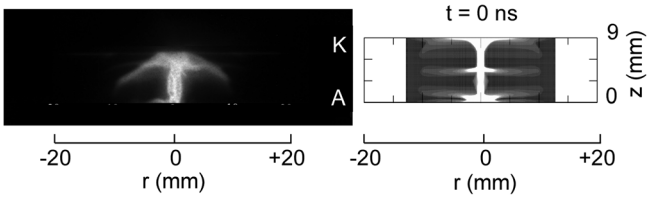


FIG. 3. Similar to Fig. 2 but only at stagnation for simulation run B where the breakdown was assumed to occur at the outermost radius (23.5 mm) of the measured density in Fig. 1.

run B requires slightly less total mass to get an implosion time within the experimental range. Despite the close agreement of these two curves, the line density for the two runs at the time of peak K-shell emission, denoted by $m^p(z,A)$ and $m^p(z,B)$, are quite distinct. The smaller diameter of the outer shell and the slight bend in $m^o(z,A)$ for $z > 5$ mm, as well as the density perturbations along $r \sim 20$ mm generate a large Rayleigh-Taylor (R-T) bubble seen in the trough of $m^p(z,A)$ around $z = 6$ mm, and a large flare on the cathode side as seen in the bottom comparison of Fig. 2. On the other hand, the density tail beyond $r = 20$ mm along the full axial length in run B bifurcates the bubble, and leads to a spike at mid-$z$ instead of an arching flare on the cathode side. In the outermost regions of the gas puff the development of the R-T instability is sensitive to the spatial density profile and the temporal current rise.[23] There are likely shot-to-shot density fluctuations in these regions that are below the PLIF detection limit. The reproducible visible morphology in the experiments is consistent with an electrical breakdown along a reproducible density profile.

### B. Stagnation properties

During stagnation the region of K-shell emission from the simulation varies in time over an axial extent from $z \sim 4$ to $\sim 8$ mm. The experimental data during stagnation are taken from the region $4 < z < 6$ mm. We likewise analyze the simulations over the same region. The results presented in the figures below are from run A described above. In order to highlight some features, we will occasionally refer to a run C that has the same breakdown condition as run A, but

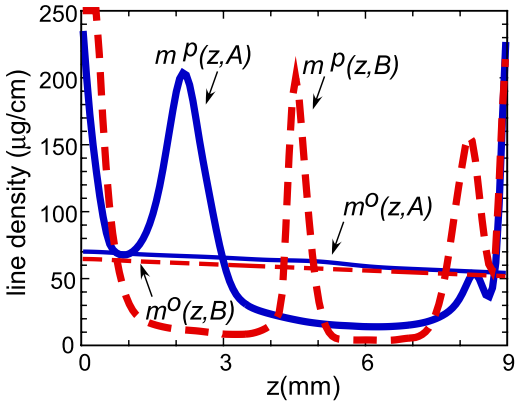


FIG. 4. The line density as a function of axial extent at the time of breakdown [$m^o(z,A)$ = thin blue line] and at the time of peak K-shell emission [$m^p(z,A)$ = thick blue line] for run A of Fig. 2. Likewise for run B of Fig. 3 [$m^o(z,B)$ = thin red dashed line; $m^p(z,B)$ = thick red dashed line].

with a uniformly higher mass (by 9%) such that the implosion occurs 497 ns after the capacitor discharge. The visible morphology of run C is negligibly different from run A in Fig. 2, but the peak current is up to 550 kA.

Figure 5 shows the time variation of the K-shell radius ($r_K$) during stagnation, for the data and run A. Specifically, $r_K$ is the radial position where the K-shell emission falls to 10% of its peak value at each separate time, based on K-shell images for the data and the escaping K-shell power for the simulation. In the data $r_K$ increases to a distinct maximum at $t = 0$ and subsequently decreases sharply late in stagnation. For the simulation, the radius at peak power is not as large, but the early and late time behavior is similar to the data.

Figure 6 compares the computed $n_e$ with the experimental data during stagnation. At $t = -5$ ns, the computed $n_e$ is negligible but rapidly rises to a peak of $\sim 10.4 \times 10^{20}$ cm$^{-3}$ by $t = 0$, and then falls off. The computed mean charge state ($\bar{Z}$) in Fig. 6 is fairly constant during stagnation, indicating that the rapid evolution of the electron density is due to compression, not ionization. This electron density is evaluated by averaging the density weighted by the escaping K-shell power over the cylindrical volume contained within $4 < z < 6$ mm. The experimental value for $n_e$ during stagnation is $6 \pm 3 \times 10^{20}$ cm$^{-3}$. It is determined from the ratio of Ly$_\alpha$ satellite lines and thus is also weighted by the K-shell emission. For the discussion below on ion temperatures, it is important to note that the reported experimental value for $n_e$ from Ref. 12 holds for times $> -2$ ns. After this time, the computed value slightly exceeds the data range around the time of peak emission.

The computed and experimental K-shell pulse ($P_K$) from the region $4 < z < 6$ mm is also displayed in Fig. 6. The peak K-shell emission for run A [$I_p$(A) = 8.15 GW] is a little over the experimentally averaged value of $6.5 \pm 1.5$ GW, and it is not as broad, especially after +2 ns. The computed K-shell yield is 24 J while the data is $25 \pm 8$ J. The time of peak K-shell power is the same as that of the peak $n_e$. While the computed K-shell pulse shape follows that of $n_e$, the intensity is very sensitive to $T_e$ because the electron

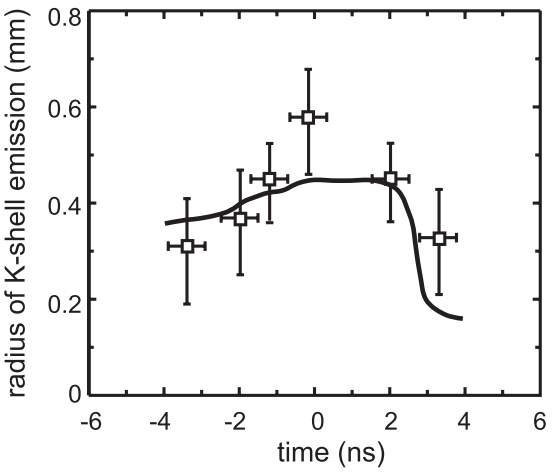


FIG. 5. Computed radius of the K-shell emitting region during stagnation (line) for run A compared with the data (symbols). Model and data are for the region $4 < z < 6$ mmm, and $t = 0$ is the time of peak K-shell emission from this region.

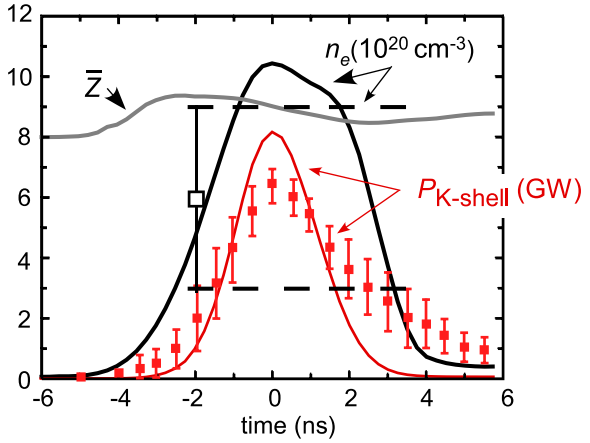


FIG. 6. Computed electron density ($n_e$ = thick black line) and charge state ($\bar{Z}$ = thick grey line) during stagnation for run A. The range for the experimental data is demarked by the thick dashed horizontal lines and applies for $t > -2$ ns. The computed K-shell pulse ($P_K$ = thin red line) and the corresponding data (red symbols). The region and time are the same as in Fig. 5. Data from Ref. 2.

temperature during stagnation is ~5 times smaller than the excitation energies of the K-shell lines. Consider the Ne Ly$_\alpha$ line of excitation energy 1021.96 eV whose intensity would scale as $(n_e^2/\bar{Z})\exp(-1021.96/T_e)$ in the optically thin limit. For run A, $T_e = 185.1$ eV at the instant of peak $n_e$ and $\bar{Z} = 9$. For run C, the peak of $n_e$ ($11.6 \times 10^{20}$ cm$^{-3}$) is larger than for run A, but its peak power is less [$I_p$(C) = 6.85 GW], as is its $T_e$ (171.6 eV) and $\bar{Z}$ (8.9). Using the above values, the peak Ly$_\alpha$ intensity of run C should be ~0.81 of run A, which is consistent with $I_p$(C)/ $I_p$(A). The above optically thin estimate is presented to highlight the sensitivity of the K-shell emission in this range of temperatures. Actually, the Ly$_\alpha$ line is optically thick for both runs A and C at the time of peak K-shell power. The detailed excitation and radiative transport are accounted for in the simulations.

The last comparison of the simulations is with the ion thermal, ion effective and electron temperature data shown as symbols in Fig. 7. $T_i$ and $T_e$ from the simulation are

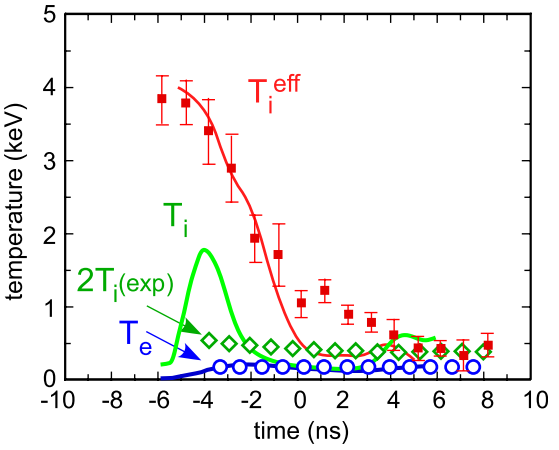


FIG. 7. Computed electron temperature ($T_e$ = blue line), thermal ion temperature ($T_i$ = green line), and effective ion temperature ($T_i^{eff}$ = red line) for run A. The data are shown as symbols ($T_e$ = circles; $T_i$ = diamonds; $T_i^{eff}$ = solid squares) in the corresponding colors. Note that $T_i$ for the data is multiplied by 2 for clarity. Data from Ref. 12.

computed in the same manner that $n_e$ was in Fig. 6. Before $-2$ ns, the computed $T_i$ is significantly larger than the results from Kroupp *et al.*[12] The rise in the computed $T_i$ reflects the thermalization of the radially inward velocity as the plasma stagnates. After $-2$ ns there is equilibration of the ion and electron thermal temperatures, as seen in the data. Our $T_e$ rises from 163 eV at $-4$ ns, peaks at 238 eV at $-2.3$ ns, and then falls steadily reaching 150 eV at $+2$ ns. The spectral modeling for $T_e$ in Kroupp *et al.*, finds a lower $T_e$ throughout the stagnation and a peak of $\sim$200 eV at $t = 0$. In either case, the electron temperature does not vary significantly throughout the stagnation because the collisional excitation of, and radiation from, K-shell levels acts as a strong thermostat.

To compute $T_i^{eff}$ from the simulations we performed an analogous procedure to that used in the experiment, namely extracting $T_i^{eff}$ from the line width of the singlet Ly$_\alpha$ satellite ($2p^2\ ^1D_2 \rightarrow 1s2p\ ^1P_1$). Doubly excited states are not included in our rad-hydro simulations, so we post-processed the output conditions. From the simulations, populations of singly excited He-like levels ($1s2s\ ^3S_1$, $1s2p\ ^3P_{0,1,2}$, $1s2p\ ^1P_1$) and the H-like ground level are known and taken as fixed, and we calculated the population of $2p^2\ ^1D_2$ in all of the computational zones at each time step under Collisional-Radiative Equilibrium (CRE) conditions. This approximation assumes that the populations of the doubly excited states are small. The kinetic processes include electron collisional excitation rates from, and radiative decay rates to, He-like states, and auto-ionization to the H-like ion. These rates were determined from the FAC atomic physics code. Detailed balancing was used to obtain collisional de-excitation rates and dielectronic capture.[24] For $T_e \sim 200$ eV, the dominant source of the doubly excited states is this last process; hence, the Ly$_\alpha$ satellite emission samples the H-like population of the plasma. Using these populations for the $2p^2\ ^1D_2$ level, the optically thin radiative transfer equation was solved for the singlet Ly$_\alpha$ satellite line along a number of parallel rays normal to the $z$-axis and passing through the region $4 < z < 6$ mm. The radial velocity was taken to vary linearly between zone interfaces, where the velocity is carried in the Mach2 code. The projection of the local flow velocity onto the ray direction produces a Doppler shift in the emission profile. The photon energy grid over which the transport is calculated was sufficiently dense to capture shifts of a few km/s. The transport was calculated for an intrinsically Gaussian emission line profile that accounted only for thermal broadening and Doppler shifts. A Voigt profile with natural broadening would include the auto-ionization rate, which is large for the $^1$D satellite line ($2.8 \times 10^{14}$ s$^{-1}$), but gives an enhanced line width not reflective of just thermal and velocity effects. Once the calculated profiles along the rays are summed together, we determine $T_i^{\rm eff}$ from the resulting synthetic profile: $\text{FWHM} = 2\sqrt{\ln 2}\sqrt{2k_B T_i^{eff}/m_i}(E_o/c)$, where $E_o$ is the line center energy (1003.52 eV), $c$ is the speed of light, $m_i$ is the mass of the Ne ion, and $k_B$ is the Boltzmann constant. After $-5$ ns, the synthetic profiles are nearly Gaussian in shape. The results shown in Fig. 7 follow the data quite closely early in the stagnation phase for $t < -1$ ns. Simulations with different load masses show the same trend but the exact curve for $T_i^{\rm eff}$ is not reproduced. For instance, for run C the $T_i^{\rm eff}$ is lower than that shown by $\sim$700 eV at early times. In both cases though, the simulated $T_i^{\rm eff}$ is less than the data for the later phase of the stagnation.

## IV. DISCUSSION

The results in Fig. 7 raise two questions for discussion. (i) Why does the thermal ion temperature in the simulation differ from the data, while (ii) the effective ion temperatures agree? Regarding the first question, recall the analysis of the experiment used a $n_e$ of $6 \times 10^{20}$ cm$^{-3}$ from Ly$_\alpha$ satellite intensity ratios determined for $t > -2$ ns and $T_e \sim 200$ eV. Before this time, the intensities are too weak to obtain a confident ratio. For these values, the ion-electron thermal equilibration time, $\tau_{eq} = (m_i/3m_e)\tau_{ie} \propto T_e^{3/2}/\bar{Z}n_e$, is $\sim$0.1 ns.[25] The measured $T_i^{eff}$ was used in $dT_i^{eff}/dt = -(T_i - T_e)/\tau_{eq}$ to find that $T_i \approx T_e$. According to Fig. 6, however, the computed density rapidly evolves early in the stagnation phase. Thus, the complete ion thermal energy equation is required

$$\frac{D}{Dt}\left(\frac{3}{2}\frac{n_e}{\bar{Z}}k_B T_i\right) + p_i\vec{\nabla}\cdot\vec{v} + \cdots = -\frac{n_e}{\tau_{eq}}k_B(T_i - T_e),$$

where the coefficient of the thermal equilibration term on the right hand side scales as $n_e^2$. When $n_e$ is small ($t < -2$ ns), "$p{\cdot}dV$" work and shocks heat the ions but not the electrons because equilibration is slow. After $-2$ ns, $n_e$ increases rapidly and thermal equilibration becomes effective, as seen in Fig. 6, in agreement with the data.

Regarding the second question we refer to Fig. 8, which shows the number density of H-like Ne ($n_H$), $T_i$, and the absolute value of the inward radial velocity ($|v_r|$) from run A as a function of radius for four different times during stagnation. These values are averaged over the axial extent $4 < z < 6$ mm at each radius, and for the latter two quantities weighted as done for the electron density in Fig. 6 and thermal temperatures in Fig. 7. The maximum velocity in the simulation is $\sim$180 km/s. Kroupp *et al.*, reported a higher velocity, 230 km/s based on splitting in the $^1$D satellite line at $-3.8$ ns. We also found splitting but at $-6$ ns where $T_i$ is low (Fig. 7) and the implosion has not yet thermalized. In Fig. 8 one sees that $n_H$ increases by almost two orders of magnitude during the stagnation, while $T_i$ and $|v_r|$ decrease. At $-4$ ns the highest value of $n_H$ occurs near the axis where the ion thermal temperature and radial velocity are large. One can show that the velocities and temperatures at this time are sufficient to produce multi-keV values for $T_i^{eff}$. To illustrate, consider two identical parcels of plasma moving toward each other at velocities $\pm v$. Then, along the direction of velocity the spectral separation of the two thermally broadened profiles of temperature $T_i$ at the far points demarking the individual HWHM would be $2\sqrt{\ln 2}\sqrt{2k_B T_i/m_i}(E_o/c) + 2|v|(E_o/c)$. If the velocity is $\sqrt{\ln 2}$ times the thermal speed, then these points are at the FWHM of the combined profile and one finds $T_i^{eff} = 4T_i$. Near $r \sim 0.12$ mm in Fig. 8 for $-4$ ns, $T_i \sim 2$ keV and the radial velocity is $\sim$110 km/s, nearly the same as $\sqrt{\ln 2}$ times the ion thermal speed. For individual parcels at this position and

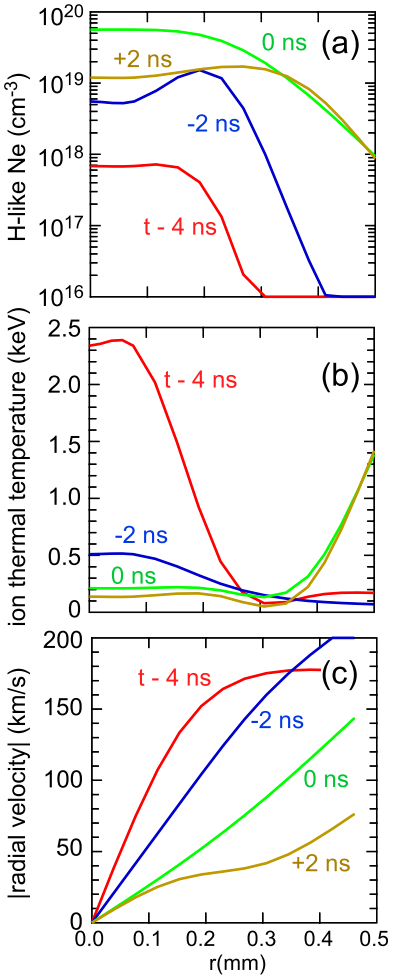


FIG. 8. (a) H-like number density, (b) thermal ion temperature, and (c) absolute value of the inward radial velocity at four times during stagnation from simulation run A.

time, one would have $T_i^{eff} \sim 8$ keV. Transport through all of the plasma reduces $T_i^{eff}$ because there are other gas parcels moving at lower velocities projected along the line of sight. By $-2$ ns in Fig. 8, the radial position of the peak in $n_H$ still has substantial velocity, but the thermal temperature is low. Thus, a smaller $T_i^{eff}$ results. As the stagnation continues through the time of peak K-shell emission, the change of $T_i^{eff}$ reflects the decreasing velocity. The rising $T_i$ late in time beyond 4 mm radius does not affect $T_i^{eff}$ because the density is low and the spectral profile of the $Ly_\alpha$ satellites is dominated by the region of high density where $T_i$ and $|v_r|$ are low.

For completeness, we note that the simulation results in Figs. 7 and 8 depend somewhat on the grid resolution, which was $128\times128$ for these figures. At a lower resolution, $96(r)\times128(z)$, the radial velocities and the ion thermal temperatures for $t<0$ are significantly less than displayed in Fig. 8. The trend in $T_i^{eff}$ at the lower resolution is similar to that in Fig. 7, but consequently its values are about 1.5 keV less prior to $-2$ ns. At higher resolution, $160(r)\times128(z)$, the radial velocities are very close to that in Fig. 8 throughout the stagnation while the ion thermal temperatures are larger. All cases used a radially moving grid. We find that the present resolution converges and trends to the experimental data, but as is typical for numerical simulations, the exact numbers vary with the resolution.

We summarize two primary conclusions of the analysis in this paper. First, we found in Figs. 1 and 2 a dramatic difference in the visible morphology of the Ne gas puff implosion depending on the assumed breakdown location. If the pinch is initiated at the radius where the density first increases through the Paschen minimum ($r \sim 20$ mm), then the observed images could be reproduced with a single arching flare on the cathode side. If initiated at the outer radius of the PLIF data beyond the Paschen minimum, the R-T instability is altered by the low density gas and leads to prominent spikes that are not observed. The second conclusion developed from Figs. 6–8 is that the large $T_i^{eff}$ determined from spectral line widths in the studied experiment arise solely from a combination of strong gradients in the radial velocity as well as the high ion thermal temperature resulting from the dissipation of this velocity. Both of the above conclusions strictly apply only to the Ne gas puff experiments under study and were possible because of the extensive data set that enabled a careful validation of the Mach2-TCRE simulation code used here. These conclusions may be relevant to the other earlier reports of high temperatures from line widths listed in Table I. For current research, the analysis on gas breakdown and $T_i^{eff}$ may be relevant for gas puff experiments with Ne on the Cobra generator at Cornell University[26] and with Ar on the Z generator at Sandia National Laboratories.[27]

We close with a review of two approximations intrinsic to the simulations. First, the calculations were performed under the condition of CRE, meaning in particular that the ionization kinetics is assumed to be in equilibrium, i.e., time independent. In Fig. 6, the plasma transitions from He-like to H-like over the time $-5 < t < -3$ ns while the electron density is quite low, $<3\times10^{20}$ cm$^{-3}$. Reference to the discussion in Thornhill *et al.*[28] suggests that this ionization step could take longer than 2 ns. Time dependent kinetics in-line with a multi-dimensional MHD pinch simulation would be a major challenge. If this were included we conjecture that the temporal separation between the rise in the electron density and the peak K-shell power would be greater than the $\sim$4 ns of Fig. 6. In other words, the time of peak power would be delayed relative to the rise of the electron density. The discrepancy between the computed thermal ion temperature at $-4$ ns and the experimental results in Fig. 7 is possibly connected to this missing physics. If $n_e$ rapidly increased $\sim$6 ns before peak power, then the rise and fall of the ion thermal temperature in Fig. 7, i.e., the thermalization, would precede the data. The curve for $T_i^{eff}$ would shift earlier but still follow the trend in the data. The second intrinsic approximation is that our 2D $r$-$z$ simulations have only axial and radial velocities, and the latter must be zero on the $z$-axis. Nevertheless the simulations reproduced the observed trends in the magnitude and temporal variation of $T_i^{eff}$, i.e., without recourse to 3D effects, rotation, or small scale turbulence. This does not mean that we can rule out such hydrodynamic motion in pinches, particularly in pinches that display significant azimuthal asymmetry. Time dependent kinetics and complex motion during stagnation will likely play a key role in the

understanding of high atomic number K-shell source development, such as Kr on the Z generator.

## ACKNOWLEDGMENTS

This work was supported by the U.S. Department of Energy, National Nuclear Security Administration, and by the U.S.-Israel Binational Science Foundation.

[1]B. Jones, C. A. Coverdale, C. Deeney, D. B. Sinars, E. M. Waisman, M. E. Cuneo, D. J. Ampleford, P. D. LePell, K. R. Cochrane, J. W. Thornhill, J. P. Apruzese, A. Dasgupta, K. G. Whitney, R. W. Clark, and J. P. Chittenden, Phys. Plasmas **15**, 122703 (2008).
[2]C. A. Coverdale, C. Deeney, A. L. Velikovich, R. W. Clark, Y. K. Chong, J. Davis, J. Chittenden, C. L. Ruiz, G. W. Cooper, A. J. Nelson, J. Franklin, P. D. LePell, J. P. Apruzese, J. Levine, J. Banister, and N. Qi, Phys. Plasmas **14**, 022706 (2007).
[3]M. E. Cuneo, M. C. Herrmann, D. B. Sinars, S. A. Slutz, W. A. Stygar, R. A. Vesey, A. B. Sefkow, G. A. Rochau, G. A. Chandler, J. E. Bailey, J. L. Porter, R. D. McBride, D. C. Rovang, M. G. Mazarakis, E. P. Yu, D. C. Lamppa, K. J. Peterson, C. Nakhleh, S. B. Hansen, A. J. Lopez, M. E. Savage, C. A. Jennings, M. R. Martin, R. W. Lemke, B. W. Atherton, I. C. Smith, P. K. Rambo, M. Jones, M. R. Lopez, P. J. Christenson, M. A. Sweeney, B. Jones, L. A. McPherson, E. Harding, M. R. Gomez, P. F. Knapp, T. J. Awe, R. J. Leper, C. L. Ruiz, G. W. Cooper, K. D. Hahn, J. McKenney, A. C. Owen, G. R. McKee, G. T. Leifeste, D. J. Ampleford, E. M. Waisman, A. Harvey-Thompson, R. J. Kaye, M. H. Hess, S. E. Rosenthal, and M. K. Matzen, IEEE Trans. Plasma Sci. **40**, 3222 (2012).
[4]J. P. Apruzese, K. G. Whitney, J. Davis, and P. C. Kepple, J. Quant. Spectrosc. Radiat. Transfer **57**, 41 (1997).
[5]N. D. Ouart, A. S. Safronova, V. L. Kantsyrev, A. A. Esaulov, K. M. Williamson, I. Shresths, G. C. Osborne, and M. E. Weller, IEEE Trans. Plasma Sci. **38**, 631 (2010).
[6]T. W. L. Sanford, T. J. Nash, R. C. Mock, R. B. Spielman, K. W. Struve, J. H. Hammer, J. S. De Groot, K. G. Whitney, and J. P. Apruzese, Phys. Plasmas **4**, 2188 (1997).
[7]K. L. Wong, P. T. Springer, J. H. Hammer, C. A. Iglesias, A. L. Osterheld, M. E. Foord, H C. Burns, J. A. Emig, and C. Deeney, Phys. Rev. Lett. **80**, 2334 (1998).
[8]J. S. Levine, P. L. Coleman, B. H. Failor, J. C. Riordan, Y. Song, H. M. Sze, C. A. Coverdale, C. Deeney, J. S. McGurn, J. P. Apruzese, J. Davis, B. Moosman, J. W. Thornhill, A. L. Velikovich, B. V. Weber, D. Bell, and R. Schneider, Phys. Plasmas **8**, 533 (2001).
[9]M. G. Haines, P. D. LePell, C. A. Coverdale, B. Jones, C. Deeney, and J. P. Apruzese, Phys. Rev. Lett. **96**, 075003 (2006).
[10]E. Kroupp, D. Osin, A. Starobinets, V. Fisher, V. Bernshtam, Y. Maron, I. Uschmann, E. Förster, A. Fisher, and C. Deeney, Phys. Rev. Lett. **98**, 115001 (2007).
[11]Y. Fan, L. Zheng-Hong, Q. Yi, J. Shu-Qing, X. Fei-Biao, Y. Jian-Lun, X. Rong-Kun, and J. Yongh-Jie, Chinese Phys. B **19**, 075204 (2010).
[12]E. Kroupp, D. Osin, A. Starobinets, V. Fisher, V. Bernshtam, L. Weingarten, Y. Maron, I. Uschmann, E. Förster, A. Fisher, M. E. Cuneo, C. Deeney, and J. L. Giuliani, Phys. Rev. Lett. **107**, 105001 (2011).
[13]M. G. Haines, AIP Conf. Proc. **1088**, 57 (2009).
[14]D. Osin, E. Kroupp, A. Starobinets, G. Rosenweig, D. Alumot, Y. Maron, A. Fisher, E. Yu, J. L. Giuliani, and C. Deeney, IEEE Trans. Plasma Sci. **39**, 2392 (2011).
[15]R. E. Peterkin, M. H. Frese, and C. R. Sovinec, J. Comput. Phys. **140**, 148 (1998).
[16]A. L. Velikovich, J. L. Giuliani, S. T. Zalesak, J. W. Thornhill, and T. A. Gardiner, Phys. Plasmas **19**, 012707 (2012).
[17]J. W. Thornhill, J. P. Apruzese, J. Davis, R. W. Clark, A. L. Velikovich, J. L. Giuliani, Y. K. Chong, K. G. Whitney, C. Deeney, C. A. Coverdale, and F. L. Cochran, Phys. Plasmas **8**, 3480 (2001).
[18]J. P. Apruzese and J. L. Giuliani, J. Quantum Spectrosc. Radiat. Transfer **111**, 134 (2010).
[19]J. P. Apruzese, J. L. Giuliani, and S. B. Hansen, High Energy Density Phys. **8**, 231 (2012).
[20]D. E. Osterbrock, *Astrophysics of Gaseous Nebulae* (Freeman, San Francisco, 1974), p. 19.
[21]M. F. Gu, Can. J. Phys. **86**, 675 (2008).
[22]Y. P. Razier, *Gas Discharge Physics* (Springer-Verlag, Berlin, 1991), p. 134.
[23]A. L. Velikovich, F. L. Cochran, and J. Davis, Phys. Rev. Lett. **77**, 853 (1996).
[24]A. V. Vinogradov, I. Yu. Skobelev, and E. A. Yukov, Sov. Phys. JETP **45**, 925 (1977).
[25]S. I. Braginskii, in *Reviews of Plasma Physics*, vol. 1, edited by A. Leontovich (Consultants Bureau, New York, 1965), p. 205.
[26]P. A. Gourdain, R. J. Concepcion, M. T. Evans, J. B. Greenly, D. A. Hammer, C. L. Hoyt, E. Kroupp, B. R. Kusse, Y. Maron, A. S. Novick, S. A. Pikuz, N. Qi, G. Rondeau, E. Rosenberg, P. C. Shrafel, C. E. Seyler, and T. C. Shelkovenko, Nucl. Fusion **53**, 083006 (2013).
[27]B. Jones, C. A. Jennings, D. C. Lamppa, S. B. Hansen, A. J. Harvey-Thompson, D. J. Ampleford, M. E. Cuneo, T. Strizic, D. Johnson, M. C. Jones, N. W. Moore, T. M. Flanagan, J. L. McKenney, E. M. Waisman, C. A. Coverdale, M. Krishnan, P. L. Coleman, K. W. Elliott, R. E. Madden, J. Thompson, A. Bixler, J. W. Thornhill, J. L. Giuliani, Y. K. Chong, A. L. Velikovich, A. Dasgupta, and J. P. Apruzese, "A renewed capability for gas puff science on Sandia's Z machine," IEEE Trans. Plasma Sci. (to be published).
[28]J. W. Thornhill, K. G. Whitney, J. Davis, and J. P. Apruzese, J. Appl. Phys. **80**, 710 (1996).